Quantifying supraglacial debris-related melt-altering effects on the Djankuat Glacier, Russian Federation, Part 2: Using a modelling approach to derive the glacier-specific Østrem curve

Yoni Verhaegen[1], Oleg Rybak[1,2,3], Victor V. Popovnin[4], and Philippe Huybrechts[1]

[1]*Departement Geografie, Vrije Universiteit Brussel, Pleinlaan 2, 1050 Brussels, Belgium*

[2]*Water Problems Institute, Russian Academy of Sciences, Gubkina Str. 3, 119333 Moscow, Russia*

[3]*Kabardino-Balkarian State University, Chernyshevskogo Str. 173, 360004, Nalchik, Russia*

[4]*Department of Geography, Lomonosov Moscow State University, 1 Leninskiye Gory, 119991 Moscow, Russia*

Corresponding author: Yoni Verhaegen (yoni.verhaegen@vub.be) (ORCHID ID 0000-0002-0164-2086)

Key Points:

- We use a spatially distributed and physically based energy and mass balance model to derive the Østrem curve for the Djankuat Glacier.
- Sub-debris melt rates are enhanced for debris thinner than 9 cm, but melt is increasingly suppressed for thicker debris layers.
- The eventual debris-related melt modification is shaped by both the debris thickness, its properties and the local climatic conditions.

Key Words:

- glacier
- debris cover
- ice
- cryosphere
- numerical modelling
- climate change

Abstract

We used a spatially distributed and physically based energy and mass balance model to derive the Østrem curve, that is the supraglacial debris-related relative melt alteration versus the debris thickness, for the Djankuat Glacier, Caucasus, Russian Federation. The model is driven by meteorological input data from two on-glacier automatic weather stations and ERA-5 reanalysis data. A direct pixel-by-pixel comparison of the melt rates obtained from both a clean ice and debris-covered ice mass balance model results in the quantification of debris-related relative melt-modification ratios, capturing the degree of melt enhancement or suppression as a function of the debris thickness. In doing so, our model is the first attempt to derive the glacier-specific Østrem curve through spatially distributed energy and mass balance modelling. The main results show that a maximum relative melt enhancement occurs on the Djankuat Glacier for thin and patchy debris with a thickness of 3 cm. However, insulating effects suppress sub-debris melt under debris layers thicker than a critical debris thickness of 9 cm. Sensitivity experiments show that especially within-debris properties, such as the thermal conductivity, the vertical porosity gradient, and the moisture content of the debris pack, highly impact the magnitude of the sub-debris melt rates.

Plain Language Summary

The presence of rocks, boulders and sediments on top of glacier ice can significantly modify the behavior of mountain glaciers. As such, when compared to a clean ice surface, a debris-covered ice surface is subject to debris-related modified melting regimes. In our study, we quantify this melt-modification effect for the Djankuat Glacier, a well-studied glacier situated in the Caucasus. The results are expressed by a so-called Østrem curve, that quantifies the debris-related melt-modification effect and compares it to the corresponding debris thickness. Here, we present the first attempt to construct such a glacier-specific Østrem curve through sophisticated 2D energy and mass balance modelling. Our results show that ice melt is enhanced for thin and patchy debris layers, whereas melt is increasingly suppressed for thick and continuous debris layers due to an insulating effect. The degree of melt modification and the shape of the Østrem curve are found to depend on the debris properties, its moisture content, its spatio-temporal distribution, and the local climatic conditions. Quantifying such melt-modification effects is important to more accurately understand and assess the behavior of (partly) debris-covered glaciers under a future warming climate.

1 Introduction

Recently, a lot of attention has been given to assessing and modelling the presence of a supraglacial debris cover (i.e. a cover of rocks, boulders and sediments on top of the ice) on mountain glaciers, especially due to the observed sharp worldwide increase of the supraglacial debris-covered areas and its increasingly important impact on glacier behavior within the current changing climate (e.g. Glasser et al., 2016; Scherler et al., 2018; Herreid and Pellicciotti, 2020). The increase of the supraglacial debris cover has been noted in many regions of the world (Scherler et al., 2018) but has been especially remarkable in the Caucasus region, as its total area increased from 48.3 ± 3.1 km^2 in 1986 to 79.0 ± 4.9 km^2 in 2014 (Tielidze et al., 2020). Scherler et al. (2018) even conclude that the Caucasus region holds the highest percentage of debris-covered glacier surfaces worldwide. Because changing melting patterns of (sub-debris) glacier ice affect eventual glacier-related global sea level contributions (e.g. Fox-Kemper et al., 2021), impacts the risk for glacio-geomorphological hazardous threats (e.g. Chernomorets et al., 2018), and serves as an important factor for water resource management for many populated places (e.g. Hagg et al., 2010; Huss and

Hock, 2018; Fyffe et al., 2019), the need to incorporate the melt-altering effects of supraglacial debris into glacier models has increased greatly (Huo et al., 2021; Winter-Billington, 2022; Compagno et al., 2022). To assess the future water supply, it is therefore important to pinpoint the available glacial water resources and evaluate their melting rate in a warming climate.

The presence of debris on the glacier surface can significantly influence the melting patterns of mountain glaciers, depending on the debris area and thickness, its physical and geometrical properties, its moisture content and the local climatic conditions (e.g. Østrem, 1959; Nicholson and Benn, 2006; Reid and Brock, 2010; Anderson and Anderson, 2016; Miles et al., 2022; Verhaegen et al., subm.). A slight relative melt enhancement seems to occur under thin debris, but ice melt and glacier retreat can be drastically suppressed if sufficiently thick debris is present over a large portion of a glacier (e.g. Reid and Brock, 2010; Evatt et al., 2015; Verhaegen et al., 2020; Rounce et al., 2021; Ferguson and Vieli, 2021). Glacier-specific debris-related relative melt-altering effects are often expressed by a so-called Østrem curve, which quantifies the ratio of sub-debris melt to clean ice melt as a function of the debris thickness at a fixed location (Østrem, 1959). The derivation of such a curve is crucial in determining the influence of supraglacial debris on the melt and climate change response of a mountain glacier. However, since a direct comparison of clean ice and debris-covered ice melt is not straightforward and requires an abundant amount of input data and model variables, the derivation of such an Østrem curve through spatially distributed mass balance modelling is still absent in the literature. Few studies have attempted to derive a glacier-specific Østrem curve, but have either (1) used scattered data from ablation stake measurements obtained during field work to construct the curve, hence failing to incorporate data from the entire debris-covered glacier surface, (2) suffered from the inability to directly compare clean ice and debris-covered ice melt at the same location, hence failing to derive relative melt ratios, (3) have derived the Østrem curve from modelling experiments for one single point on the glacier (e.g. by varying hypothetical debris thickness values at the location of an automatic weather station), (4) neglected or were unable to include the relative melt enhancement for thin debris in the Østrem curve, or (5) did not include varying effective debris properties with depth to construct the curve, which often deviates from real world conditions (e.g. Tangborn and Rana, 2000; Popovnin and Rozova, 2002; Reid and Brock, 2010; Wei et al. 2010; Wang et al., 2011; Brook et al., 2013; Dohbal et al., 2013; Juen et al., 2014; Ragettli et al., 2015; Carenzo et al., 2016; Anderson et al., 2021; Steiner et al., 2021; Compagno et al., 2022).

In this research, we focus on deriving the relationship between supraglacial debris-related relative melt-altering effects and the debris thickness for the Djankuat Glacier, a partly debris-covered World Glacier Monitory Service (WGMS) reference glacier (North Caucasus, Russian Federation). A 2D spatially distributed and physically based energy and mass balance model for both the clean ice and the debris-covered ice areas of the Djankuat Glacier is therefore used (Verhaegen et al., subm.). The main objectives are (1) to use the model to derive the glacier-specific Østrem curve for the Djankuat Glacier, and (2) to determine the sensitivity of sub-debris

melt and debris-related melt-altering effects to key parameters and local climatic conditions. In doing so, the model attempts to address the earlier-mentioned limitations of previous work.

2 Location, data and models

2.1 The Djankuat Glacier and its supraglacial debris cover

The Djankuat Glacier (43°12′N, 42°46′E) is a partly debris-covered temperate valley glacier situated in the Caucasus, near the border of the Russian Federation and Georgia (Fig. 1). Annually repeated observations since 1967 CE have revealed a significant shrinkage of the glacier area over the years due to an increasingly negative cumulative surface mass balance (e.g. Popovnin and Naruse, 2005; Lavrentiev et al., 2014; Rets et al., 2019; WGMS 2022). For 2020 CE conditions, satellite imagery revealed that the glacier occupied an area of ca. 2.30 km^2 and had a length of ca. 3.1 km when taking from its highest point near the Djantugan peak.

On the other hand, both the glacier-averaged debris thickness h_d (ca. +0.010 m yr^{-1}) and the debris-covered area A_d (ca. +0.006 km^2 yr^{-1}) on the glacier have increased significantly. During the most recent debris survey in 2010 CE, the glacier-averaged debris thickness was estimated to be 0.54 m, and about 13% of the glacier's surface area was covered with debris (Popovnin et al., 2015). Recent observations have shown the increasingly noticeable impact of the supraglacial debris on the glacier. As such, the quasi-fully debris-covered western part of the snout retreated significantly slower than the less covered eastern part, resulting in a length difference between both sides of ca. 180 m in 2010 and ca. 250 m for 2020 CE conditions. Based on the extrapolation of these debris area and thickness trends, and the anticipated continued climate warming, the supply of debris onto the Djankuat Glacier is believed to increase further in the future as long as the glacier does not retreat beyond the debris sources (Popovnin et al., 2015).

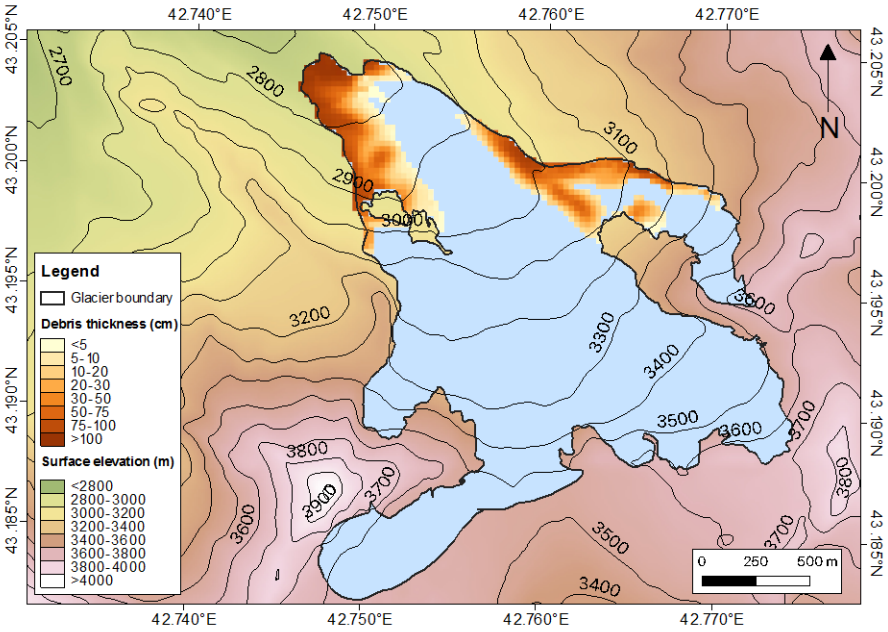

Figure 1. Sketch of the Djankuat Glacier for 2010 CE conditions with debris thickness map (after Popovnin et al., 2015).

2.2 Surface energy and mass balance model

The 2D physically based energy and mass balance model for the Djankuat Glacier is taken from Verhaegen et al. (subm.) and considers the difference between accumulation ACC and runoff RO during the entire 2008/09 measurement year and is driven by climatic input data (air temperature, precipitation, wind speed, relative humidity, atmospheric transmissivity and the sky emissivity) from 2 on-glacier Automatic Weather Stations (AWSs), the Terskol meteo station, and is supplemented with ERA5-Land data (Verhaegen et al. (subm.)). The local surface mass balance b_a is:

$$b_a = \int_{yr} (ACC - RO)dt \tag{1}$$

The model assumes that accumulation (ACC) only depends on the occurrence of solid precipitation (P_s). The runoff (RO) is determined as:

$$RO = \begin{cases} W_s & if\ h_s > 0 \\ M & if\ h_s = 0 \end{cases} \tag{2}$$

Hence, in the case of snow on the surface (a snow depth $h_s > 0$), runoff is calculated as the meltwater outflow from a saturated snowpack W_s, following Schaefli and Huss (2011). For snow-free conditions ($h_s = 0$), runoff RO is considered equal to the melt M. The corresponding melt M of snow (M_s), clean ice (M_i) and debris-covered ice (M_d) is calculated as:

$$M = \begin{cases} M_s & if\ h_s > 0 \\ M_i\left(\frac{A_d - A}{A}\right) + M_d\left(\frac{A_d}{A}\right) & if\ h_s = 0 \end{cases} \tag{3}$$

where A_d is the debris-covered area and A_d/A the fractional debris-covered area, for which an empirical formula was derived for the Djankuat Glacier (Verhaegen et al., subm.):

$$\frac{A_d}{A} = 1 - \frac{1}{(5.901 * exp(0.0607 * h_d) - 5.576} + 0.000286 \tag{4}$$

where the debris thickness h_d is expressed in cm.

2.2.1 Modelling snow and clean ice melt

In the case of snow or ice, the energy available for melting Q_M is calculated as the residual of the surface energy balance (Verhaegen et al., subm.):

$$\begin{aligned} Q_M = S_\downarrow(1-\alpha_s)\tau + \varepsilon_a\sigma T_a^4 - \varepsilon_s\sigma T_s^4 + c_a\rho_a C_E u(T_a - T_s) + L_v\rho_a C_E u(q_a - q_s) \\ + \rho_w c_w P(T_a - T_s) \end{aligned} \tag{5}$$

Here, $S_\downarrow$ is the downward solar radiation, α the surface albedo, τ the sky transmissivity, ε the emissivity, σ the Stefan-Boltzmann constant, c the specific heat capacity, ρ the density, T the temperature, u the wind speed, C_E the turbulent exchange coefficient, P the precipitation rate, L_v the latent heat of evaporation, and q the specific humidity. Subscripts "a", "s" and "w" stand for air, surface, and water respectively. The first term on the right-hand site of Eq. 5 denotes the net shortwave radiation Q_S, the second and third term the net longwave radiation Q_L, the fourth and fifth term the sensible (Q_{SH}) and latent heat fluxes (Q_{LH}) respectively, and lastly, the sixth term represents the heat flux due to rainfall Q_R.

Melt rates for snow M_s and clean ice M_i are calculated using the energy available for melt, which is determined by a sophisticated surface energy balance model (Verhaegen et al., subm.):

$$M_s|\, M_i = max\left(0, \frac{Q_M \Delta t}{\rho_w L_m}\right) \quad (6)$$

where ρ_w is the density of water, L_m the latent heat of fusion and Δt the model time step.

2.2.2 Modelling sub-debris ice melt

2.2.2.1 Governing equations

The sub-debris melt model starts from the energy balance equation at the debris surface:

$$S_{\downarrow}(1-\alpha_d)\tau + \varepsilon_a \sigma T_a^4 - \varepsilon_d \sigma T_s^4 + c_a \rho_a C_E u(T_a - T_s) + L_v \rho_a C_E u(q_a - q_s) + \rho_w c_w P(T_a - T_s) + k_d \frac{\partial T_d}{\partial z} = 0 \quad (7)$$

where k is the thermal conductivity. The last term on the left denotes the conductive heat flux, which is absent for snow and clean ice melt in Eq. 5. The subscript "d" here refers to the debris pack. Beneath the surface layer, the change of the internal energy within the debris pack is defined by the thermodynamic heat equation:

$$\rho_d c_d \frac{\partial T_d}{\partial t} = \frac{\partial}{\partial z}\left(k_d \frac{\partial T_d}{\partial z}\right) + \rho_w c_w P\left(\frac{\partial T_d}{\partial z}\right) + \rho_a c_a C_E u\left(\frac{\partial T_d}{\partial z}\right) + L_v\left(\frac{\partial E_d}{\partial z}\right) + \frac{\partial \varphi_d}{\partial z} \quad (8)$$

where φ is the net radiation flux and E the evaporation rate. Subsurface debris temperature changes can thus be driven by the five modes of heat transfer that are summed up at the right-hand side of Eq. 8: conduction (term 1), advection (term 2), convection (term 3), phase changes (term 4) and radiative transfer (term 5). Since sub-debris wind speeds are negligible for debris thicker than a few cm (Evatt et al., 2015), the convection term on the right-hand side of Eq. 8 is assumed negligible. Below the debris surface, radiative heat transfer furthermore becomes insignificant as radiation cannot easily penetrate rock (Reid and Brock, 2010), so that the fifth term on the right-hand side of Eq. 8 is left out in our model as well. All terms have units J m^{-3} s^{-1}.

2.2.2.2 Effective debris properties

In Eqs. 7 and 8, the debris properties ρ, c, and k have been converted from "whole rock" properties (subscript r) to "effective" (subscript d) debris properties. A dependency of the debris thermal properties to the porosity (ϕ_d) and the moisture content (θ_d) is therefore considered. Following Collier et al. (2015) and Steiner et al. (2021), the debris characteristics are derived as weighted functions of whole-rock values and the contents of the pore spaces. Consequently, the debris volumetric heat capacity is calculated as:

$$\rho_d c_d(z) = \rho_r c_r(1-\phi_d(z)) + \left(\rho_w c_w\left(\frac{\theta_d(z)}{\phi_d(z)}\right) + \rho_a c_a\left(1 - \frac{\theta_d(z)}{\phi_d(z)}\right)\right)\phi_d(z) \quad (9)$$

The effective thermal conductivity k_d is calculated likewise:

$$k_d(z) = k_r(1-\phi_d(z)) + \left(k_w\left(\frac{\theta_d(z)}{\phi_d(z)}\right) + k_a\left(1 - \frac{\theta_d(z)}{\phi_d(z)}\right)\right)\phi_d(z) \quad (10)$$

The debris porosity ϕ_d decreases linearly with depth due to a vertical debris porosity gradient γ_{ϕ_d}, resulting in depth-dependent effective debris properties (Verhaegen et al., subm.):

$$\phi_d(z) = \phi_d - 0.33\left(\frac{z}{h_d}\right) \quad (11)$$

where h_d is the debris thickness and z is the debris depth (i.e. 0 at the surface and h_d at the bottom), which results in a porosity ϕ_d of 43% and 10% at the top and bottom respectively.

2.2.2.3 Within-debris moisture retention

In the case that within-debris water retention occurs, the water depth w_d in a vertical debris sublayer is determined from the balance between input and output:

$$\frac{\partial w_d}{\partial t} = M_i + W_s + P - W_d - \Phi_d \quad (12)$$

where we assume that the input of liquid moisture depends on ice melt (M_i) at the bottom, and liquid precipitation (P) and meltwater outflow from a saturated snowpack (W_s) at the surface.

We implement a simplified water percolation scheme which assumes that whenever liquid water enters the debris, it initially occupies the lowermost layer (on top the impermeable ice-debris interface) until local saturation is reached. Hereafter, moisture is allowed to accumulate in the next deepest unsaturated layer, and as such may gradually decrease the depth of the saturated horizon relative to the debris surface, as moisture accumulates within the debris pack. Note that this simplified scheme ignores a physically based quantification of the vertical debris water fluxes of percolating water, which would, in our opinion, add more detail than warranted for our study. Moisture output is governed by a depth-dependent within-debris runoff-related sink term W_d:

$$W_d = max\left(0, w_d - \left(\frac{w_d}{t_d}\right)\right) \quad (13)$$

Here, w_d is the sublayer water depth ($w_d = \theta_d h_d$) and t_d is a depth-dependent runoff parameter (Reijmer and Hock, 2008; Collier et al., 2014; Giese et al., 2020). The term t_d acts as a runoff timescale, defining the number of timesteps needed to drain a debris sublayer and as such determines the corresponding vertical distribution of moisture:

$$t_d = t_{min} + (t_{max} - t_{min}) * \left(\frac{exp\left(t_t \frac{z}{h_d}\right)}{exp(t_t)}\right) \quad (14)$$

where t_{min}, t_{max} and t_t are tunable parameters. Giese et al. (2020) reports typical values for the runoff-related parameters t_{min} = 1 h, t_{max} = 48 h, and t_t = 30. Apart from runoff, an additional evaporation and condensation term Φ_d (m s^{-1}) is also included in Eq. 12 to account for the phase changes within the debris pack:

$$\Phi_d = \frac{E_d}{\rho_w} = \frac{Q_{LH}}{\rho_w L_v} \quad (15)$$

The calculation scheme of Q_{LH} is then implemented according to a reservoir approach, similar to Collier et al. (2014). In this case, the surface specific humidity in Eq. 7 includes a correction factor that implicitly incorporates within-debris evaporative cooling effects:

$$q_s = q_s^* \left(\frac{\sum_{i=1}^{N} \theta_{d,i}}{\sum_{i=1}^{N} \phi_{d,i}} \right) \quad (16)$$

with q_s^* the saturated specific humidity of the surface. The correction term therefore varies between 0 and 1 and depends on the total fraction of void spaces filled with water within the debris sublayers.

Due to the high number of unknown variables in Eqs. 12 to 14, the within-debris phase changes term of Eq. 8 are initially neglected in our model. From now on, we thus assume a dry debris pack in which no within-debris water retention occurs and where all moisture input is immediately removed by runoff. This reduces the right-hand side of Eq. 8 to the first 2 terms (conduction and advection by percolating rain). Since θ_d = 0, Eqs. 9 and 10 are also reduced to only consider air-filled pore spaces, which now corresponds to the dry debris model used in Verhaegen et al. (subm.). We will, however, later on determine the effect of within-debris water retention on the Østrem curve by arbitrarily varying the extent of moisture input and output into the debris pack through Eqs. 12 to 14 (see section 4.3).

2.2.2.4 Calculation of sub-debris melt

The energy for melting $Q_M^{\downarrow}$ at the debris-ice interface finally results from the conductive heat flux at the base of the debris and the heat added or removed by infiltrating rainwater:

$$Q_M^{\downarrow} = Q_C^{\downarrow} + Q_R^{\downarrow} \quad (17)$$

where $Q_R^{\downarrow}$ is the heat advected (added or removed) by percolating rainwater. The term $Q_C^{\downarrow}$ is the conductive heat flux at the bottom layer of the debris, which depends on the effective debris properties (k_d, ρ_d and c_d) and the internal debris temperature (T_d) at the vertical ice-debris margin. Sub-debris melt rates M_d are eventually calculated using the energy available for melt:

$$M_d = max\left(0, \frac{Q_M^{\downarrow} \Delta t}{\rho_w L_m}\right) \quad (18)$$

Hence, in the case of a debris cover, the conductive flux at the base of the debris and the heat added or removed by percolating rainwater provide the energy available for melting $Q_M^{\downarrow}$.

2.2.3 Model calibration and validation

The model was calibrated by minimizing the root mean square error (RMSE) between observed and modelled local surface mass balances, and the model validation procedures showed satisfying results. A more extensive description of the energy and mass balance model and its construction, calibration and validation can be found in the accompanying paper Verhaegen et al. (subm.).

3 Deriving the Østrem curve

To quantify the melt-altering effects versus debris thickness on the Djankuat Glacier, we ran both the calibrated clean ice and debris-covered ice mass balance model throughout the 2008/09 measurement year using the parameters listed in Table 2 of Verhaegen et al. (subm.). For the clean ice SMB model, we set the debris thickness over the entire glacier area to 0, as if there were no debris present. The SMB outcome from both models is then directly compared, so that pixel-by-pixel debris-covered ice melt versus clean ice melt ratios M_d/M_i could be derived (Fig. 2).

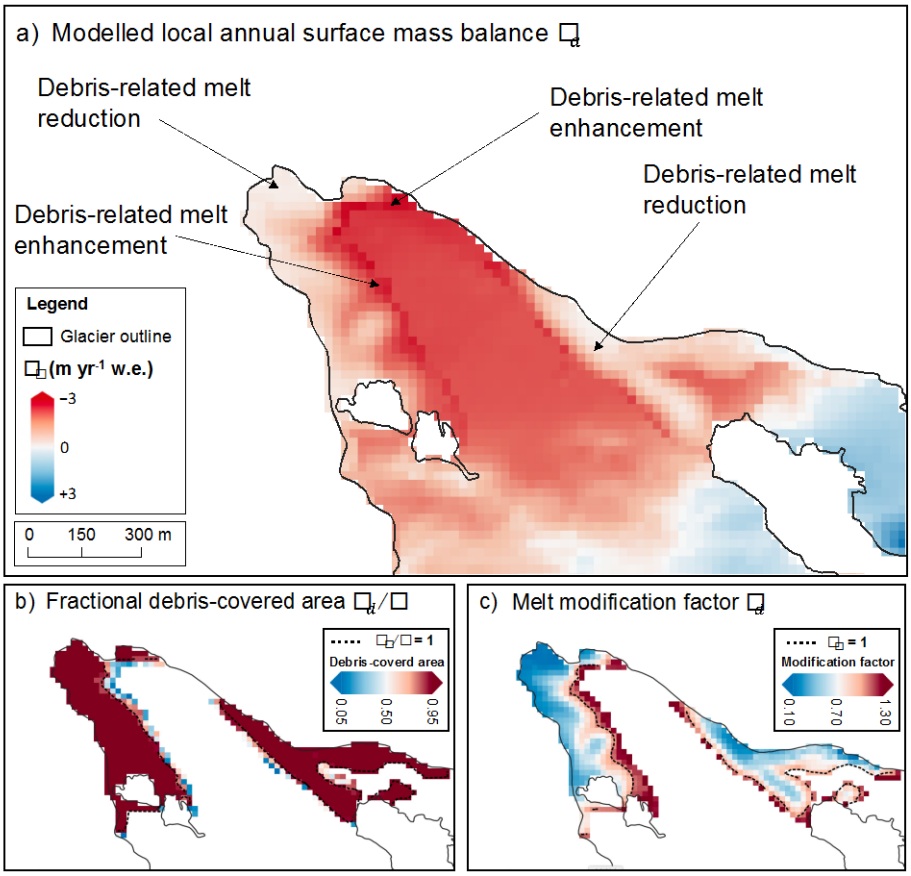

Figure 2. The (a) modelled (calibrated) surface mass balance (SMB) in the ablation area of the Djankuat Glacier during the 2008/09 balance year, (b) the pixel-by-pixel fractional debris-covered area, and (c) the modelled relative melt modification ratio (M_d/M_i).

After plotting the obtained melt ratios against the debris thickness itself (Fig. 3a), values for the critical (i.e. the debris thickness for which the sub-debris melt is equal to that of clean ice, h_d^c) and characteristic debris thickness (i.e. the debris thickness at which the melt rate is e^{-1} (~ 37%) of the clean ice melt, h_d^*) could be assigned to the debris thickness that exhibited a value for the melt ratio closest to 1 and 0.37 respectively. The effective debris thickness (i.e. the debris thickness of maximum ice ablation, h_d^e) and the associated maximum melt enhancement factor (f_d^e) were determined by locating the maximum of a polynomial function through all values between h_d = 0 cm and $h_d = h_d^c$. To then fit an equation to the Østrem curve itself, we used a linear equation for values of $h_d \leq h_d^e$ (between points [0,1] and [h_d^e,f_d^e]), and a reciprocal equation for $h_d > h_d^e$, which has been shown to provide the optimal fit for a Østrem curve (Rounce et al., 2021; Nicholson et al., 2021), see Fig. 3b.

After deriving the pixel-by-pixel relative melt ratios from both the clean ice SMB and debris-covered ice SMB model, their values could be directly compared to the corresponding debris thickness at that pixel. The result is shown in Fig. 3, where the best empirical fit was found with:

$$\frac{M_d}{M_i} = f_d = \begin{cases} 1 + 0.12 * h_d & if\ h_d \le h_d^e \\ \dfrac{1.66201}{(1 + 0.05415 * h_d)} - 0.10533 & if\ h_d > h_d^e \end{cases} \quad (19)$$

where M_d/M_i is the supraglacial debris-related relative ice melt ratio. A melt enhancement subsequently occurs for thin and patchy debris, while a typical reciprocal-type decrease of the relative melt can be seen as the debris further thickens. The effective and critical debris thicknesses are found to exhibit values of 3 and 9 cm respectively on the Djankuat Glacier, and at the effective debris thickness, ice melt is enhanced with a factor f_d^e of 1.36 according to our study. The characteristic debris thickness is, at last, modelled to be 44 cm. For thick debris, the melt becomes highly suppressed and gradually decays to negligible when the value approaches 200 cm. According to Eq. 19 melt equals 0 at a debris thickness of 272 cm. Outliers in Fig. 3a are all situated near the accumulation zone, where the effects of faster snow melt on debris-covered surfaces overtakes the effect of the relative melt-modification.

The obtained Østrem curve produced by our model exhibits the typical features that are generally associated with a melt-modification versus debris thickness relationship. The occurrence of a maximum melt enhancement for thin debris, followed by a reciprocal decay of the sub-debris melt rates as debris thickens, therefore highlights the findings of previous research (e.g. Østrem, 1959; Reid and Brock, 2010; Evatt et al., 2015; Rounce et al., 2021).

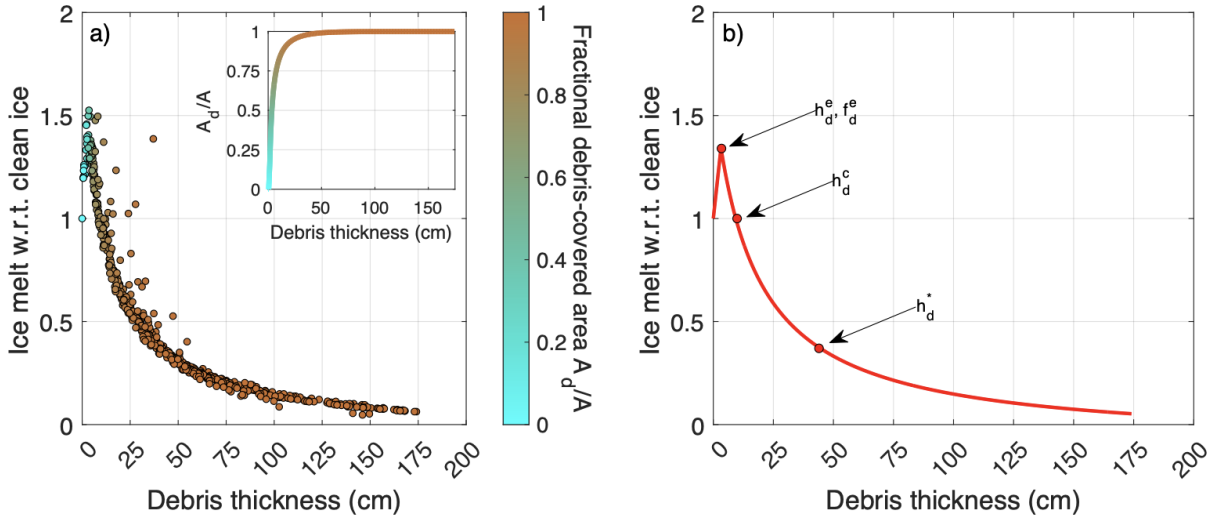

Figure 3. The (a) pixel-by-pixel modelled debris thickness vs. the relative melt modification factor and (b) the corresponding best fit to the Østrem curve for the Djankuat Glacier in this study. Shown in (b) are the corresponding effective (h_d^e), critical (h_d^c), and characteristic (h_d^*) debris thickness and the maximum melt enhancement factor f_d^e.

4 Sensivity experiments

4.1 Sensitivity to debris-related parameters

By means of sensitivity experiments, the change of magnitude of the sub-debris melt rate and the shape of the Østrem curve with respect to five debris-related key parameters (k_d, C_E, γ_{ϕ_d}, α_d, and

ε_d) was analyzed by increasing or decreasing either one of the parameters by 5% and 10% respectively, while keeping the other four constant at their chosen or calibrated values.

The results indicate that the sub-debris melt is especially sensitive to changes of the thermal conductivity k_d ($\Delta M_d/\Delta k_d$ = +0.076 m yr^{-1} w.e. 10%$^{-1}$) and the debris cover porosity gradient γ_{ϕ_d} ($\Delta M_d/\Delta \gamma_{\phi_d}$ = +0.045 m yr^{-1} w.e. 10%$^{-1}$), whereas sub-debris melt rates are slightly less, but still significantly, sensitive to the variations of the turbulent exchange coefficient C_E ($\Delta M_d/\Delta C_E$ = -0.029 m yr^{-1} w.e. 10%$^{-1}$), the debris surface emissivity ($\Delta M_d/\Delta \varepsilon_d$ = -0.022 m yr^{-1} w.e. 10%$^{-1}$) and the debris albedo α_d ($\Delta M_d/\Delta \alpha_d$ = -0.015 m yr^{-1} w.e. 10%$^{-1}$). Hence, higher values for k_d and a stronger porosity gradient γ_{ϕ_d} are shown to significantly increase sub-debris melt rates due to a more efficient thermal conduction (inset Fig. 4). In that case, the Østrem curve shifts to the right and the shielding effect of the debris is less efficient. The ratio M_d/M_i consequently increases for a given debris thickness, which results in higher values for f_d^e, h_d^e, h_d^c, and h_d^*. On the other hand, higher values for C_E, ε_d and α_d decrease sub-debris melt rates (inset Fig. 4). In that case, the Østrem curve shifts to the left, implying lower values for f_d^e, h_d^e, h_d^c, and h_d^*.

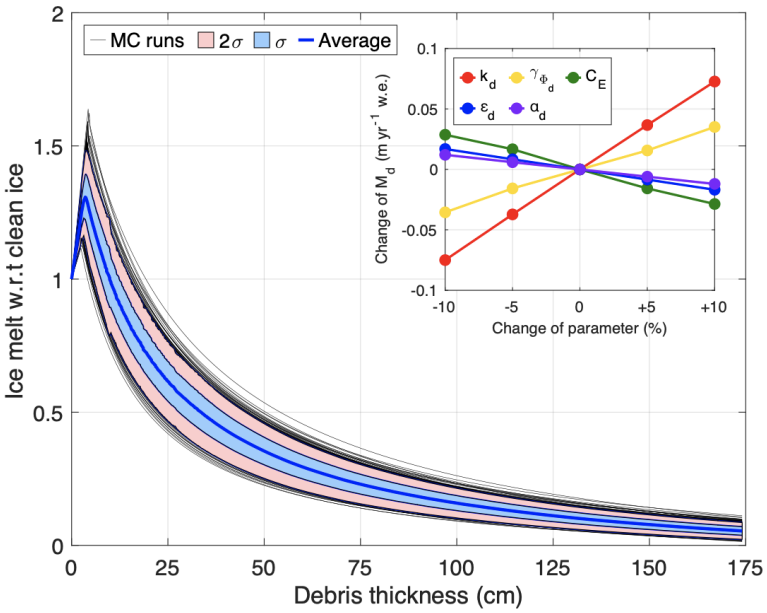

Figure 4. The resulting Østrem curves from 1,000 Monte Carlo (MC) model simulations with varying debris properties, shown with the average curve and the shaded standard deviation intervals. Decreasing (increasing) sub-debris melt rates shift the Østrem curve to the left (right). The inset on the right shows the sensitivity of the sub-debris melt rates to five debris-related parameters.

As an additional sensitivity and uncertainty assessment procedure, a total of 1,000 Monte Carlo simulations were executed with the sub-debris melt model. Therefore, a set of assumed normally distributed values for the key debris property parameters was created, for which values range between -50% and +50% of the best fit or chosen value. As such, 1,000 simulations were conducted to generate a probability density function of the Østrem curve for the Djankuat Glacier, from which general statistics were determined (Fig. 4). The pattern shows that the effective debris thickness h_d^e across all 1,000 runs has a mean value of 3.5 $\pm$ 1.5 cm, for which the sub-debris melt

is enhanced by a factor 1.31 $\pm$ 0.08. The critical debris thickness h_d^c is modelled to have a value of 9.9 $\pm$ 2.4 cm and the characteristic debris thickness, at last, is found to be 48.3 $\pm$ 7.4 cm. These values closely resemble the characteristics of the Østrem curve that resulted from the model calibration (section 3). It is furthermore important to note that the sensitivity to varying debris properties decreases with an increasing debris thickness. This finding is presumably related to the enhanced attenuation of the net energy flux through thicker debris (e.g. Fyffe et al., 2014; Winter-Billington, 2022).

4.2 Sensitivity to local climatic conditions

Local climatic conditions are believed to impact the Østrem curve as well (e.g. Reznichenko et al., 2010; Miles et al., 2022). We investigated the influence of changing climatic conditions on the melt modification-debris thickness relationship by producing various Østrem curves after artificially perturbating the three main meteorological variables (air temperature, relative humidity and wind speed) with a fixed amount throughout the 2008/09 measurement year.

4.2.1 Air temperature

The air temperature perturbations ΔT_a were all positive in accordance with an expected future warming climate (e.g. Masson-Delmotte et al., 2021). For all scenarios, the corresponding values for the effective, critical and characteristic debris thickness were modelled to decrease, as the model outcome suggests values for, on average, $\Delta h_d^e/\Delta T_a$ = -0.13 cm °C^{-1}, $\Delta h_d^c/\Delta T_a$ = -0.35 cm °C^{-1}, and $\Delta h_d^*/\Delta T_a$ = -1.44 cm °C^{-1}. The maximum melt enhancement factor changes according to $\Delta f_d^e/\Delta T_a$ = -0.006 °C^{-1} (Fig. 5). As such, for a temperature increase of +5°C, which is the order of magnitude of the increase that can be expected for a SSP5-8.5 scenario by 2071-2100 AD, the effective, critical and characteristic debris thickness have decreased to ca. 2 cm, 7 cm and 41 cm respectively, while the maximum melt enhancement slightly decreased to a factor 1.32.

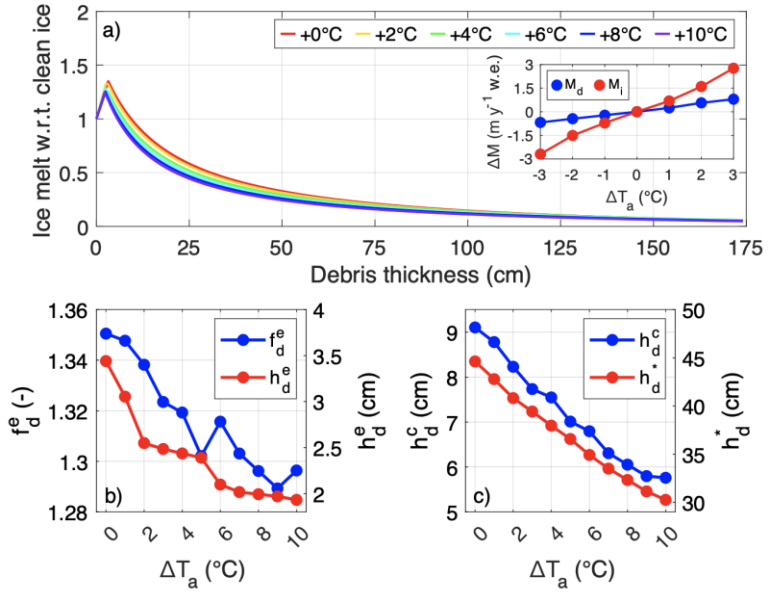

Figure 5. The (a) modelled influence of positive temperature perturbations on the shape of the Østrem curve for the Djankuat Glacier. Subplots (b) and (c) show the effect of the perturbation on the maximum melt enhancement factor (f_d^e), as well as on the effective (h_d^e), critical (h_d^c), and characteristic (h_d^*) debris thickness. The inset in (a) shows the corresponding curves for $\Delta M_d/\Delta T_a$ and $\Delta M_i/\Delta T_a$.

A relationship between the characteristic debris thickness h_d^* and the air temperature was already proposed by Anderson and Anderson (2016) and Miles et al. (2022) and is thus confirmed by our experiments. A similar conclusion can be drawn for the effective and critical debris thickness: also h_d^e and h_d^c both exhibit lower values in a warming climate. This effect arises because $\Delta M_d/\Delta T_a$ is generally lower than $\partial M_i/\partial T_a$ due to the dampening effect of the debris cover, hence changing the ratio M_d/M_i (inset of Fig. 5). Increasing M_d alone would increase the ratio M_d/M_i for a given debris thickness and shift the Østrem curve to the right, but increasing M_i alone would decrease M_d/M_i and shift the Østrem curve to the left. Since $\Delta M_i/\Delta T_a > \Delta M_d/\Delta T_a$, the net result is that the ratio M_d/M_i overall decreases for a given debris thickness, hence shifting the Østrem curve to the left. Put into practice, this means that, although sub-debris melt and clean ice melt are both enhanced in a warmer climate, the relative melt suppression of the supraglacial debris layer becomes slightly more pronounced in a future warming climate.

4.2.2 Wind speed

Higher wind speeds increase the turbulent heat fluxes and enhance the efficiency of the surface-atmosphere interaction, hence facilitating snow and ice melt. This decreases the ratio M_d/M_i and shifts the Østrem curve to the left. In the case of debris-covered ice, the opposite effect occurs. Here, higher wind speeds tend to decrease sub-debris melt, as the increasingly efficient turbulent mixing of the air generally tends to cool the heated debris surface. When wind speeds increase, both processes therefore decrease the ratio M_d/M_i for a given debris thickness, hence shifting the Østrem curve to the left. The relative shielding effect of the debris is therefore modelled to increase with increasing wind speeds. The corresponding change of the values for the effective, critical and characteristic debris thickness with wind speed are estimated to be, on average, $\Delta h_d^e/\Delta u$ = -0.24 cm (m s^{-1})$^{-1}$, $\Delta h_d^c/\Delta u$ = -1.08 cm (m s^{-1})$^{-1}$, and $\Delta h_d^*/\Delta u$ = -4.39 cm (m s^{-1})$^{-1}$. The maximum melt enhancement factor changes according to $\Delta f_d^e/\Delta u$ = -0.042 (m s^{-1})$^{-1}$ (Fig. 6).

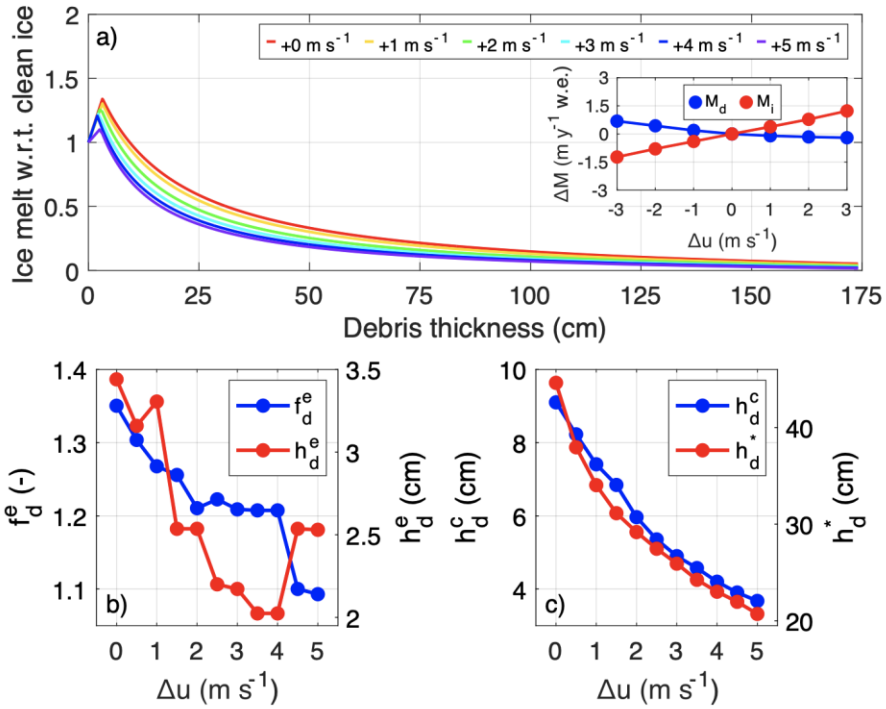

Figure 6. Same as for figure 5 but for the near-surface wind speed u.

4.2.3 Relative humidity

Increasing the relative humidity of the air also affects the eventual shape of the Østrem curve. On the one hand, increasing RH_a facilitates clean ice and snow melt through changes of the latent heat flux. As such, a higher value for RH_a decreases the efficiency of evaporation at the saturated surface, with less evaporative cooling effects and hence more energy for melt. This decreases the ratio M_d/M_i and shifts the Østrem curve to the left. In the case of debris-covered ice, an increased relative humidity of the air causes the latent heat flux between the surface and the atmosphere to become increasingly pronounced, with moisture condensing more efficiently onto the debris surface from the moist air above. The corresponding release of latent heat due to the condensation process affects the debris surface, ultimately implying more sub-debris ice melt. The effect is that the ratio M_d/M_i increases for a given debris thickness, shifting the Østrem curve to the right. Again, since $\Delta M_i/\Delta RH_a > \Delta M_d/\Delta RH_a$, the net result is a shift of the Østrem curve to the left. The corresponding change of the values for the effective, critical and characteristic debris thickness with air relative humidity are estimated to be, on average, $\Delta h_d^e/\Delta RH_a$ = -0.60 cm (10 %)$^{-1}$, $\Delta h_d^c/\Delta RH_a$ = -1.52 cm (10 %)$^{-1}$, and lastly $\Delta h_d^*/\Delta RH_a$ = -4.21 cm (10 %)$^{-1}$. The melt enhancement factor f_d^e changes according to $\Delta f_d^e/\Delta RH_a$ = -0.034 (10 %)$^{-1}$ (Fig. 7).

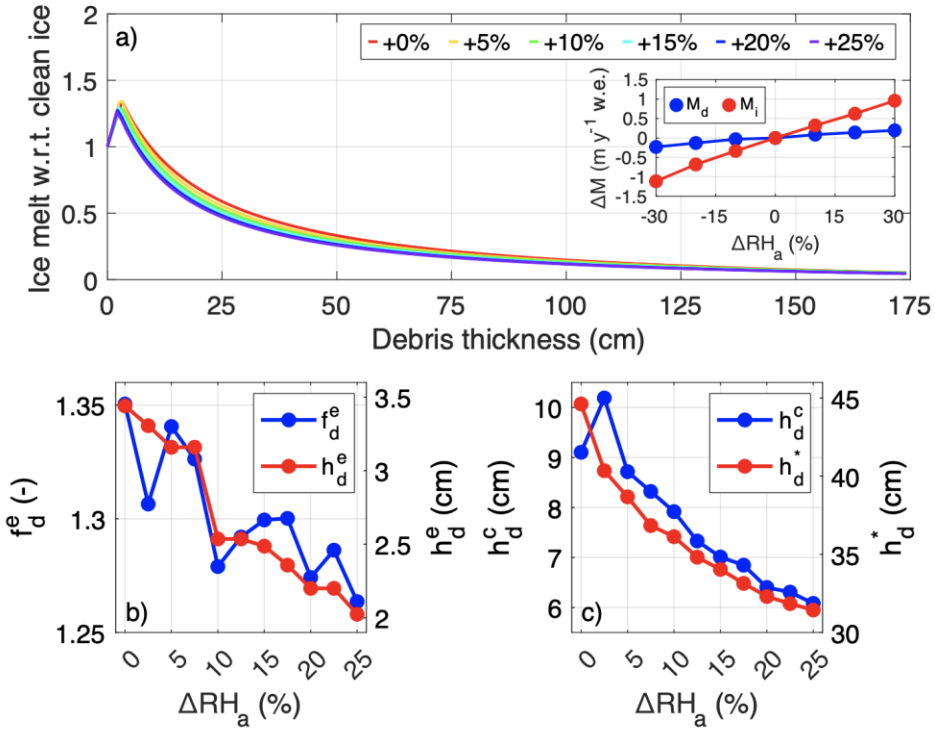

Figure 7. Same as for figure 6 but for the air relative humidity RH_a.

4.3 Effect of moisture retention

The inclusion of the simplified percolation scheme from section 2.2.2.3 with the proposed values of t_{min}, t_{max} and t_t by Giese et al. (2020) results in an almost permanently saturated bottom layer during the summer season. However, the presence of moisture at the base of the debris did not significantly influence our model results. In fact, including moisture retention in our model caused the values for f_d^e, h_d^e, h_d^c and h_d^* to change by only -0.1%, -4.7%, -5.2%, and -3.8%, respectively,

when compared to our dry debris reference model. The corresponding sub-debris melt rates have decreased only by ca. 4% on average.

We furthermore tested the effect of within-debris moisture retention on the shape of the Østrem curve by comparing the sub-debris melt beneath a completely dry debris pack (our actual model as used in this study) to a permanent partially saturated and a permanent completely saturated debris pack (Fig. 8). Here, a partially saturated debris pack involves a condition in which only the bottom layer(s) are fully saturated. The effects of moisture retention are modelled to become more pronounced with a higher degree of within-debris saturation. Especially for a higher degree of saturation, the impact on sub-debris melt changes notably. When, for example, assuming a fully water-saturated debris pack (i.e. the correction term in Eq. 16 becomes 1 and q_s equals q_s^*), the Østrem curve and the corresponding sub-debris melt rates do change significantly. This condition can be achieved by putting t_{min}, t_{max} and t_t to 1000, 1000 and 500 respectively, resulting in extreme slow runoff and a high degree of saturation in the entire vertical column. As the magnitude of heat extraction due to the latent heat flux increases greatly, the sub-debris melt rates decrease with ca. 27% on average in that case. The values for f_d^e, h_d^e, h_d^c and h_d^* change by -8.4%, -20.8%, -42.1% and -45.2% respectively, indicating a significant shift of the Østrem curve to the left (Fig. 8). As with air temperature, wind speed and the relative humidity, the effect of within-debris moisture retention decreases with an increasing debris thickness, as shown by the Østrem curves in Fig. 8.

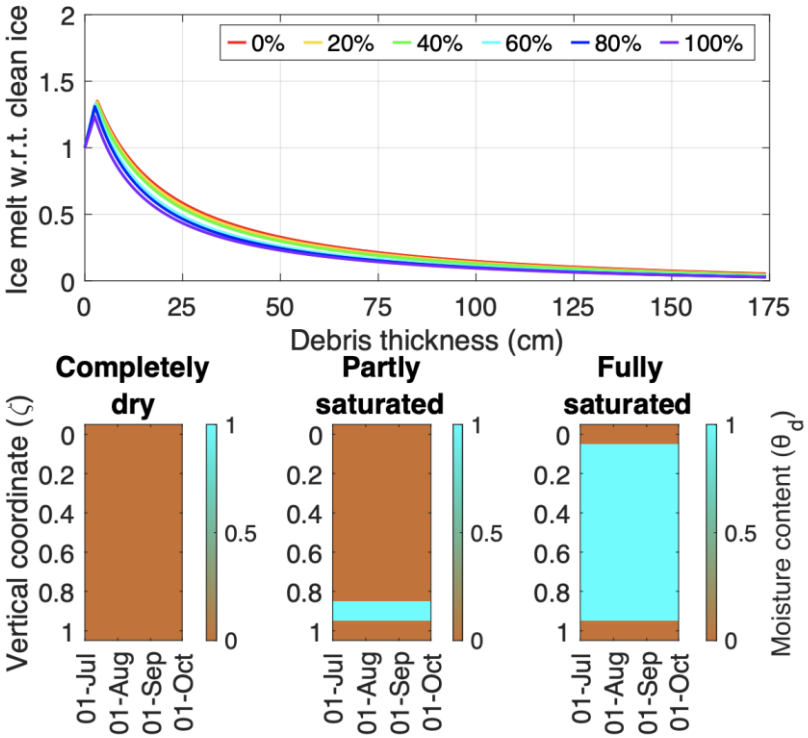

Figure 8. The (above) influence of within-debris moisture retention on the Østrem curve of the Djankuat Glacier. The three columns below visualize the degree of saturation within the debris pack in the vertical.

5 Discussion

5.1 Comparison with other glaciers

When compared to Østrem curves derived for other glaciers (e.g. Østrem, 1959; Reid and Brock, 2010; Wang et al., 2011; Brook et al., 2013; Ragettli et al., 2015; Carenzo et al., 2016; Anderson et al., 2021; Steiner et al., 2021), the melt-debris thickness relationship for the Djankuat Glacier is found to exhibit relatively high sub-debris melting rates. As such, in other studies, the effective debris thickness h_d^e is generally found within the 0-2 cm range, while typical values for the critical thickness h_d^c are usually found within the 2-5 cm range (e.g. Evatt et al., 2015; Reznichenko et al., 2010; Steiner et al., 2021). The literature furthermore suggests that the characteristic debris thicknesses h_d^* exhibits a value of only ca. 10-20 cm for most glaciers (e.g. Anderson and Anderson, 2016; Steiner et al., 2021). The respective values for h_d^e, h_d^d and h_d^* for the Djankuat Glacier are all situated outside the higher limits of the proposed intervals in the literature.

We assume that the relatively high thermal conductivity and the strong vertical porosity gradient are the most plausible determining factors in explaining this pattern, due to their ability to facilitate heat conduction, as well as their high sensitivity with respect to the sub-debris melt rates (section 4.1). Adding to this, the elevated melting rates may also be explained through the presence of nonconductive processes within the debris (e.g. Conway and Rasmussen, 2000; Evatt et al., 2015; Giese et al., 2020; Petersen et al., 2022). In our model, we, for example, included the heat added or removed by rainwater, which can impact sub-debris melt rates significantly in the relatively wet climate around the northern slope of the Main Caucasus Ridge (ca. 3000 mm yr^{-1} or more of precipitation at the highest elevations of the glacier). In our model, it is found to increase the total sub-debris melt at the AWS2 location by ca. 16% (if it is assumed that no within-debris water retention takes place). Unfortunately, data to further investigate other nonconductive processes, such as within-debris convection (e.g. Evatt et al., 2015), are lacking.

However, a direct comparison of Østrem curves from different glaciers may not be the most appropriate strategy to consider. The sensitivity experiments in our study namely point out that the magnitude of the sub-debris melt rates and the shape of the Østrem curve highly depend on the physical and geometrical debris properties (k_d, C_E, γ_{ϕ_d}, α_d, and ε_d), its moisture content (θ_d) and the local climatic conditions (T_a, RH_a and u). Changes of these parameters and/or conditions consequently imply a corresponding change of the Østrem curve. When put into practice, this implies that the effective, critical, and characteristic debris thickness may (slightly) vary in space across different regions but may also slightly change at local scales on individual glaciers, hence further complicating a direct comparison of Østrem curves of different glaciers located in different regions and at different altitudes. The outcomes of our model and the corresponding sensitivity experiments therefore indicate the need to account for site-specific debris properties, as well as for the vertical changes of these properties. It is namely striking that sub-debris melt rates are especially impacted by within-debris properties (k_d, γ_{ϕ_d} and θ_d) rather than by surface properties (α_d, ε_d and C_E), as the within-debris parameters impact the effective debris properties through the entire vertical debris column. Our model results furthermore underline the need to account for changing site-specific local climatic conditions, which can be especially important for time-dependent debris-covered glacier modelling under a future warming climate.

5.2 Model limitations, uncertainties and recommendations

The incorporation of debris properties into the model is shown to significantly affect the eventual modelled sub-debris melt rates. In our model, it should be noted that values for ρ_r, c_r, k_r, γ_{ϕ_d} and

ϕ_d are kept constant in space and time. However, it is known that debris properties may vary largely in space and time, depending primarily on the debris lithology, porosity and water content (e.g. Nicholson and Benn, 2006; Giese et al., 2020). Typical values for the density, specific heat capacity and thermal conductivity of gneiss and granite-type rocks are suggested to be 2670 kg m^{-3}, 770 J kg^{-1} K^{-1} and 3.3 W m^{-1} K^{-1} in the literature (Robertson, 1988; Gupta, 2003). In the case of schists, which have been found on the Djankuat Glacier, the thermal properties also depend on the geometric relationship between the direction of the heat flux and that of the schist planes. Since our experiments have shown that sub-debris melt is especially highly sensitive to changes of the within-debris properties, the proper choice of these parameters is subsequently important for sub-debris melt modelling. It is therefore assumed that including the spatial variability the debris properties may presumably have a significant impact on the eventual results and hence needs to be considered when assessing the results of our research. If doing so, however, an abundant amount of field data would be required, which is out of scope for this study.

The inclusion of the vertical porosity gradient in our model is furthermore particularly valuable, as many earlier studies have assumed constant debris properties with depth (e.g. Reid and Brock, 2010; Foster et al., 2012; Rounce et al., 2018), which may be significantly different from real-world conditions. Although hard to quantify and validate, the inclusion of a porosity gradient certainly needs to be assessed in future debris-covered glacier modelling, together with changing debris properties with depth in general. In our study, the incorporation of a porosity gradient allows the model to produce a good agreement between simulated and observed values. Moreover, the sub-debris melt rates show a rather high sensitivity to changes of the porosity gradient. The inclusion of varying debris properties with depth, as done in this study by means of a porosity gradient and the inclusion of a percolating water scheme, therefore certainly opens opportunities for more sophisticated debris-covered glacier models.

It must, at last, be noted that several supraglacial debris-related processes have not been included into our model. The most important of these processes include within-debris convection, meltwater pooling, within-debris refreezing of meltwater, as well as the presence of ice slopes and cliffs (e.g. Reid and Brock, 2010; Petersen et al., 2022). Especially the presence of supraglacial water bodies, bare-ice slopes and ice cliffs have been shown to potentially increase local melt rates substantially and act as local ablation hotspots (e.g. Buri et al., 2021; Lorieaux and Ruiz, 2021; Miles et al., 2022). To capture such small-scaled and detailed processes, however, high resolution input data are required at both temporal and spatial scales, which is out of scope for this study. Moreover, within-debris refreezing processes may not be significant anyway during the ablation season in low-elevation areas (Ayala et al., 2017), where most debris is located on the Djankuat Glacier.

The incorporation of debris properties into the model is shown to significantly affect the eventual modelled sub-debris melt rates. In our model, it should be noted that values for ρ_r, c_r, k_r, γ_{ϕ_d} and ϕ_d are kept constant in space and time. However, it is known that debris properties may vary largely in space and time, depending primarily on the debris lithology, porosity and water content (e.g. Nicholson and Benn, 2006; Giese et al., 2020). Typical values for the density, specific heat capacity and thermal conductivity of gneiss and granite-type rocks are suggested to be 2670 kg m^{-3}, 770 J kg^{-1} K^{-1} and 3.3 W m^{-1} K^{-1} in the literature (Robertson, 1988; Gupta, 2003). In the case of schists, which have been found on the Djankuat Glacier, the thermal properties also depend on the geometric relationship between the direction of the heat flux and that of the schist planes. Since our experiments have shown that sub-debris melt is especially highly sensitive to changes of the within-debris properties, the proper choice of these parameters is subsequently important for sub-

debris melt modelling. It is therefore assumed that including the spatial variability the debris properties may presumably have a significant impact on the eventual results and hence needs to be considered when assessing the results of our research. If doing so, however, an abundant amount of field data would be required, which is out of scope for this study.

The inclusion of the vertical porosity gradient in our model is furthermore particularly valuable, as many earlier studies have assumed constant debris properties with depth (e.g. Reid and Brock, 2010; Foster et al., 2012; Rounce et al., 2018), which may be significantly different from real-world conditions. Although hard to quantify and validate, the inclusion of a porosity gradient certainly needs to be assessed in future debris-covered glacier modelling, together with changing debris properties with depth in general. In our study, the incorporation of a porosity gradient allows the model to produce a good agreement between simulated and observed values. Moreover, the sub-debris melt rates show a rather high sensitivity to changes of the porosity gradient. The inclusion of varying debris properties with depth, as done in this study by means of a porosity gradient and the inclusion of a percolating water scheme, therefore certainly opens opportunities for more sophisticated debris-covered glacier models.

It must, at last, be noted that several supraglacial debris-related processes have not been included into our model. The most important of these processes include within-debris convection, meltwater pooling, within-debris refreezing of meltwater, as well as the presence of ice slopes and cliffs (e.g. Reid and Brock, 2010; Petersen et al., 2022). Especially the presence of supraglacial water bodies, bare-ice slopes and ice cliffs have been shown to potentially increase local melt rates substantially and act as local ablation hotspots (e.g. Buri et al., 2021; Lorieaux and Ruiz, 2021; Miles et al., 2022). To capture such small-scaled and detailed processes, however, high resolution input data are required at both temporal and spatial scales, which is out of scope for this study. Moreover, within-debris refreezing processes may not be significant anyway during the ablation season in low-elevation areas (Ayala et al., 2017), where most debris is located on the Djankuat Glacier.

6 Conclusions

In this study, a spatially distributed and physically based 2D surface energy and mass balance model at high spatial (25 m) and temporal (3-hourly) resolution was used to derive the Østrem curve (i.e. debris-related relative melt-altering effects versus debris thickness) during the 2008/09 measurement year for the Djankuat Glacier, a partly debris-covered WGMS reference glacier situated in the Caucasus (Republic of Kabardino-Balkaria, Russian Federation).

The main results show that the sub-debris ice melt is enhanced for thin and patchy debris, up to a factor f_d^e of 1.36 when compared to clean ice melt rates at a debris thickness of 3 cm. The clean ice melt was approximately equal to sub-debris melt for a critical debris thickness h_d^c of 9 cm, and a gradual reciprocal-type decay was hereafter noted, where thicker debris efficiently insulates the underlying ice and suppresses its melt significantly. The corresponding sub-debris melt rates were found to be especially sensitive to the changes of within-debris parameters and their variation with depth, such as the thermal conductivity, the porosity gradient, and its moisture content. Apart from that, changing local climatic conditions (air temperature, relative humidity, and wind speed) play a decisive role as well. The above suggests that the shape of the glacier-specific Østrem curve depends upon a complex interaction between the site-specific debris properties, the local climatic conditions, and the spatio-temporal distribution of the debris. Our results thus indicate the need to account for site-specific debris-related parameters and changing local climatic conditions during

transient debris-covered glacier modelling, as it can have a significant impact on sub-debris melt rates and the eventual shape of the Østrem curve.

In conclusion, this work presents, for the first time, a modelling approach to derive the glacier-specific Østrem curve, which is crucial in determining the effect of supraglacial debris on glacier melt patterns and its climate change response. The inclusion of varying debris properties with depth, as done in this study by means of a porosity gradient and a simple percolating rainwater scheme, opens opportunities for future debris-covered glacier modelling. Using a modelling approach, as presented here, furthermore allows capturing debris-related melt modification at the glacier-wide scale and also enables taking into account very small debris thicknesses (< 5 cm), which are typically hard to determine using in-situ methods such as ablation stake readings. Although improvements can surely be made (e.g. spatially varying debris properties, or the inclusion of the effects of other processes such as meltwater pooling, refreezing of meltwater within the debris, as well as ice slopes and cliffs), our model proves to be useful in determining the effects of supraglacial debris on sub-debris melt under changing climatic conditions. Future work should explore the effect of including glacier-specific debris-related melt-altering effects into time-dependent glacier models to determine (partly) debris-covered glacier behavior under different climate change projects and its implications for processes such as water resource management and/or glacier-related hazards (e.g. Fyffe, 2019b; Racoviteanu, 2021).

Figure captions

Figure 1. Sketch of the Djankuat Glacier for 2010 CE conditions with debris thickness map (after Popovnin et al., 2015).

Figure 2. The (a) modelled (calibrated) surface mass balance (SMB) in the ablation area of the Djankuat Glacier during the 2008/09 balance year, (b) the pixel-by-pixel fractional debris-covered area, and (c) the modelled relative melt modification ratio (Md/Mi).

Figure 3. The (a) pixel-by-pixel modelled debris thickness vs. the relative melt modification factor and (b) the corresponding best fit to the Østrem curve for the Djankuat Glacier in this study. Shown in (b) are the corresponding effective (h_d^e), critical (h_d^c), and characteristic (h_d^*) debris thickness and the maximum melt enhancement factor f_d^e.

Figure 4. The resulting Østrem curves from 1,000 Monte Carlo (MC) model simulations with varying debris properties, shown with the average curve and the shaded standard deviation intervals. Decreasing (increasing) sub-debris melt rates shift the Østrem curve to the left (right). The inset on the right shows the sensitivity of the sub-debris melt rates to five debris-related parameters.

Figure 5. The (a) modelled influence of positive temperature perturbations on the shape of the Østrem curve for the Djankuat Glacier. Subplots (b) and (c) show the effect of the perturbation on the maximum melt enhancement factor (f_d^e), as well as on the effective (h_d^e), critical (h_d^c), and characteristic (h_d^*) debris thickness. The inset in (a) shows the corresponding curves for $\Delta M_d/\Delta T_a$ and$\Delta M_i/\Delta T_a$.

Figure 6. Same as for figure 5 but for the near-surface wind speed u.

Figure 7. Same as for figure 6 but for the air relative humidity RH_a.

Figure 8. The (above) influence of within-debris moisture retention on the Østrem curve of the Djankuat Glacier. The three columns below visualize the degree of saturation within the debris pack in the vertical.

Acknowledgments

O. Rybak and V. Popovnin were supported by the Russian Science Foundation grant No. 22-17-00133. Y. Verhaegen was supported by the Copernicus Climate Change Service (C3S), which is implemented by the European Centre for Medium-Range Weather Forecasts (ECMWF) on behalf of the European Commission. The authors declare that they have no conflict of interest.

Data availability statement

The AWS data used for this study are available as open access products via the PANGAEA repository of Rets et al. (2019) (https://doi.org/10.1594/PANGAEA.894807). The model code was written in MATLAB_R2022a. It can be found and downloaded from https://github.com/yoniv1/Djankuat_Ostrem_curve (last access: 27 February 2023). (https://doi.org/10.5281/zenodo.7451031, Verhaegen and Huybrechts, subm.).

References

Anderson, L. S. and Anderson, R. S. (2016). Modeling debris-covered glaciers: response to steady debris deposition, The Cryosphere, 10, 1105–1124, https://doi.org/10.5194/tc-10-1105-2016.

Anderson, L. S., Armstrong, W. H., Anderson, R. S., and Buri, P. (2021). Debris cover and the thinning of Kennicott Glacier, Alaska: in situ measurements, automated ice cliff delineation and distributed melt estimates, The Cryosphere, 15, 265–282, https://doi.org/10.5194/tc-15-265-2021.

Ayala, A., Pellicciotti, F., Peleg, N., and Burlando, P. (2017). Melt and surface sublimation across a glacier in a dry environment: distributed energy-balance modelling of Juncal Norte Glacier, Chile, J. Glaciol., 63, 803–822, https://doi.org/10.1017/jog.2017.46.

Bozhinskiy, A. N., Krass, M. S., and Popovnin, V. V. (1986). Role of debris cover in the thermal physics of glaciers, J. Glaciol., 32, 255–266, https://doi.org/10.3189/S0022143000015598.

Brook, M. S., Hagg, W, and Winkler, S. (2013). Debris cover and surface melt at a temperate maritime alpine glacier: Franz Josef Glacier, New Zealand. New Zealand Journal of Geology And Geophysics, 56(1), 27-38. https://doi.org/10.1080/00288306.2012.736391.

Buri, P., Miles, E. S., Steiner, J. F., Ragettli, S., and Pellicciotti, F. (2021). Supraglacial Ice Cliffs Can Substantially Increase the Mass Loss of Debris Covered Glaciers, Geophysical Research Letters, 48, 150, https://doi.org/https://doi.org/10.1029/2020GL092150.

Carenzo, M., Pellicciotti, F., Mabillard, J., Reid, T., and Brock, B.W. (2016). An enhanced temperature index model for debris-covered glaciers accounting for thickness effect, Adv. Water Resour., 94, 457–469, https://doi.org/10.1016/j.advwatres.2016.05.001.

Chernomorets, S. S., Petrakov, D. A., Aleynikov, A. A., Bekkiev, M. Y., Viskhadzhieva, K. S., Dokukin, M. D., Kalov, R. K., Kidyaeva, V. M., Krylenko, V. V., Krylenko, I. V., Krylenko, I. N., Rets, E. P., Savernyuk, E. A., and Smirnov, A. M. (2018). The outburst of Bashkara glacier

627 lake (central Caucasus, Russia) on September 1, 2017, Earth's Cryosphere, 22, 70–80,
628 https://doi.org/10.21782/EC2541-9994-2018-2(61-70).

629 Collier, E., Nicholson, L. I., Brock, B. W., Maussion, F., Essery, R., and Bush, A. B. G. (2014).
630 Representing moisture fluxes and phase changes in glacier debris cover using a reservoir approach,
631 The Cryosphere, 8(4), 1429–1444, https://doi.org/10.5194/tc-8-1429-2014.

632 Collier, E., Maussion, F., Nicholson, L. I., Mölg, T., Immerzeel, W. W., and Bush, A. B. G. (2015).
633 Impact of debris cover on glacier ablation and atmosphere–glacier feedbacks in the Karakoram,
634 The Cryosphere, 9, 1617–1632, https://doi.org/10.5194/tc-9-1617-2015.

635 Compagno, L., Huss, M., Miles, E. S., McCarthy, M. J., Zekollari, H., Dehecq, A., Pellicciotti, F.,
636 and Farinotti, D. (2022). Modelling supraglacial debris-cover evolution from the single-glacier to
637 the regional scale: an application to High Mountain Asia, The Cryosphere, 16, 1697–1718,
638 https://doi.org/10.5194/tc-16-1697-2022.

639 Conway, H., Gades, A., and Raymond, C. F. (1996). Albedo of dirty snow during conditions of
640 melt, Water Resour. Res., 32, 1713–1718, https://doi.org/10.1029/96WR00712.

641 Evatt, G. W., Abrahams, I. D., Heil, M., Mayer, C., Kingslake, J., Mitchell, S. L., Fowler, A. C.,
642 and Clark, C. D. (2015). Glacial melt under a porous debris layer, Journal of Glaciology, 61, 825–
643 836, https://doi.org/10.3189/2015JoG14J235.

644 Dobhal, D., Mehta, M., and Srivastava, D. (2013). Influence of debris cover on terminus retreat
645 and mass changes of Chorabari Glacier, Garhwal region, central Himalaya, India, Journal of
646 Glaciology, 59, 961–971, https://doi.org/10.3189/2013JoG12J180.

647 Ferguson, J. C. and Vieli, A. (2021). Modelling steady states and the transient response of debris-
648 covered glaciers, The Cryosphere, 15, 3377–3399, https://doi.org/10.5194/tc-15-3377-2021.

649 Foster, L. A., Brock, B. W., Cutler, M. E. J., and Diotri, F. (2012). A physically based method for
650 estimating supraglacial debris thickness from thermal band remote-sensing data, J. Glaciol.,
651 58(210), 677–691, https://doi.org/10.3189/2012JoG11J194.

652 Fyffe, C. L., Reid, T. D., Brock, B. W., Kirkbride, M. P., Diolaiuti, G., and Smiraglia, C. (2014).
653 A Distributed Energy-Balance Melt Model of an Alpine Debris-Covered Glacier, J. Glaciol. 60,
654 587–602, https://doi.org/10.3189/2014JoG13J148.

655 Fyffe, C.L., Brock, B.W., Kirkbride, M.P., Black, A.R., Smiraglia, C. and Diolaiuti, G. (2019a).
656 The impact of supraglacial debris on proglacial runoff and water chemistry. Journal of Hydrology,
657 576, 41–57, https://doi.org/10.1016/j.

658 Fyffe, C.L., Brock, B.W., Kirkbride, M.P., Mair, D.W.F., Arnold, N.S., Smiraglia, C., Diolaiuti,
659 G., Diotri, F. (2019b). Do debris-covered glaciers demonstrate distinctive hydrological behaviour
660 compared to clean glaciers? Journal of Hydrology, 570, 584–597,
661 https://doi.org/10.1016/j.jhydrol.2018.12.069.

662 Glasser, N. F., Holt, T. O., Evans, Z. D., Davies, B. J., Pelto, M., and Harrison, S. (2016). Recent
663 Spatial and Temporal Variations in Debris Cover on Patagonian Glaciers, Geomorphology 273,
664 202–216. https://doi.org/10.1016/j.geomorph.2016.07.036.

665 Giese, A., Boone, A., Wagnon, P., and Hawley, R. (2020). Incorporating moisture content in
666 surface energy balance modeling of a debris-covered glacier, The Cryosphere, 14(5), 1555–1577,
667 https://doi.org/10.5194/tc-14-1555-2020.

Godfrey, C. M., and Stensrud, D. J. (2010). An Empirical Latent Heat Flux Parameterization for the Noah Land Surface Model, Journal of Applied Meteorology and Climatology, 49(8), 1696-1713.

Gupta, R. P. (2003). Remote Sensing Geology, Springer, New York, 656 pp.

Hagg, W., Shahgedanova, M., Mayer, C., Lambrecht, A., and Popovnin, V. V. (2010). A sensitivity study for water availability in the Northern Caucasus based on climate projections, Glob. Planet. Change, 73, 161–171, https://doi.org/10.1016/j.gloplacha.2010.05.005.

Herreid, S, and Pellicciotti, F. (2020). The state of rock debris covering Earth's glaciers. Nat. Geosci., 13, 621–7, https://doi.org/10.1038/s41561-020-0615-0.

Huo, D., Chi, Z., and Ma, A. (2021). Modeling Surface Processes on Debris-Covered Glaciers: A Review with Reference to the High Mountain Asia, Water, 13, 101, https://doi.org/10.3390/w13010101.

Huss, M. and Hock, R. (2018). Global-scale hydrological response to future glacier mass loss, Nature Climate Change, 8, 135–140, https://doi.org/10.1038/s41558-017-0049-x.

Juen, M., Mayer, C., Lambrecht, A., Han, H., and Liu, S. (2014). Impact of varying debris cover thickness on ablation: a case study for Koxkar Glacier in the Tien Shan, The Cryosphere, 8, 377–386, https://doi.org/10.5194/tc-8-377-2014.

Lavrentiev, I. I., Kutuzov S. S., Petrakov, D. A., Popov, G. A., and Popovnin, V. V. (2014). Ice thickness, volume and subglacial relief of Djankuat Glacier (Central Caucasus), Ice and Snow, 4, 7–19, https://doi.org/10.15356/2076-6734-2014-4-7-19 (in Russian).

Loriaux, T. and Ruiz, L. (2021). Spatio-Temporal Distribution of Supra-Glacial Ponds and Ice Cliffs on Verde Glacier, Chile, Frontiers in Earth Science, 9, 448, https://doi.org/10.3389/feart.2021.681071.

Masson-Delmotte, V., Zhai, P., Pirani, A., Connors, S., Péan, C., Berger, S., Caud, N., Chen, Y., Goldfarb, L., Gomis, M., Huang, M., Leitzell, K., Lonnoy, E., Matthews, J., Maycock, T., Waterfield, T., Yelekçi, O., Yu, R., and Zhou, B. E. (2021). Summary for Policymakers., In: Climate Change 2021: The Physical Science Basis. Contribution of Working Group I to the Sixth Assessment Report of the Intergovernmental Panel on Climate Change, IPCC, Cambridge University Press.

Milles, E. S., Steiner J. F., Buri, P., Immerzeel, W. W., and Pelliciotti, F. (2022). Controls on the relative melt rates of debris-covered glacier surfaces, Environ. Res. Lett., 17, 064004, https://doi.org/10.1088/1748-9326/ac6966.

Moore, P. L. (2021). Numerical Simulation of Supraglacial Debris Mobility: Implications for Ablation and Landform Genesis, Front. Earth Sci., 9, https://doi.org/10.3389/feart.2021.710131.

Nicholson, L. and Benn, D. I. (2006). Calculating ice melt beneath a debris layer using meteorological data, J. Glaciol., 52, 463–470, https://doi.org/10.3189/172756506781828584.

Nicholson, L., Wirbel, A., Mayer, C., and Lambrecht, A. (2021). The Challenge of Non-Stationary Feedbacks in Modeling the Response of Debris-Covered Glaciers to Climate Forcing, Frontiers in Earth Science, 9, https://doi.org/10.3389/feart.2021.662695.

Østrem, G. (1959). Ice melting under a thin layer of moraine, and the existence of ice cores in moraine ridges, Geogr. Ann., 41, 228–230.

Petersen E., Hock R., Fochesatto G. J., and Anderson, L. S. (2022). The Significance of Convection in Supraglacial Debris Revealed Through Novel Analysis of Thermistor Profiles, Journal of Glaciology, 127, 9, https://doi.org/10.1029/2021JF006520.

Popovnin, V. V. and Rozova, A. (2002). Influence of sub-debris thawing on ablation and runoff of the Djankuat Glacier in the Caucasus, Nord. Hydrol., 33, 75–94, https://doi.org/10.2166/nh.2002.0005.

Popovnin, V. V. and Naruse, R. (2005). A 34-year long record of mass balance and geometric changes of the Djankuat Glacier, Caucasus, Bull. Glaciol. Res., 22, 121–133.

Popovnin, V. V., Rezepkin, A. A., and Tielidze, L. G. (2015). Superficial moraine expansion on the Djankuat glacier snout over the direct glaciological monitoring period, Earth's Cryosphere, 19, No. 1, 79–87.

Racoviteanu, A.E., Nicholson L, Glasser, N. F., Miles, E., Harrison, S., and Reynolds J. (2021). Debris-covered glacier systems and associated glacial lake outburst flood hazards: challenges and prospects, Journal of the Geological Society, https://doi.org/10.1144/jgs2021-084.

Reid, T. D. and Brock, B. W. (2010). An energy-balance model for debris-covered glaciers including heat conduction through the debris layer, J. Glaciol., 56, 903–916, https://doi.org/10.3189/002214310794457218.

Reijmer, C. H. and Hock, R. (2018). Internal accumulation on Storglaciären, Sweden, in a multi-layer snow model coupled to a distributed energy and mass-balance model, Journal of Glaciology, 54, 61–72, https://doi.org/10.3189/002214308784409161.

Rets, E. P., Popovnin, V. V., Toropov, P. A., Smirnov, A. M., Tokarev, I. V., Chizhova, J. N., Budantseva, N. A., Vasil'chuk, Y. K., Kireeva, M. B., Ekaykin, A. A., Veres, A. N., Aleynikov, A. A., Frolova, N. L., Tsyplenkov, A. S., Poliukhov, A. A., Chalov, S. R., Aleshina, M. A., and Kornilova, E. D. (2019). Djankuat glacier station in the North Caucasus, Russia: a database of glaciological, hydrological, and meteorological observations and stable isotope sampling results during 2007–2017, Earth Syst. Sci. Data, 11, 1463–1481, https://doi.org/10.5194/essd-11-1463-2019.

Ragettli, S., Pellicciotti, F., Immerzeel, W., Miles, E., Petersen, L., Heynen, M., Shea, J., Stumm, D., Joshi, S., and Shrestha, A. (2015). Unraveling the hydrology of a Himalayan catchment through integration of high resolution in situ data and remote sensing with an advanced simulation model, Advances in Water Resources, 78, 94–111, https://doi.org/10.1016/j.advwatres. 2015.01.013.

Rounce, D. R., King, O., McCarthy, M., Shean, D. E., and Salerno, F. (2018). Quantifying debris thickness of debris-covered glaciers in the Everest region of Nepal through inversion of a subdebris melt model, J. Geophys. Res., 123(5), 1094– 1115, https://doi.org/10.1029/2017jf004395.

Rounce, D. R., Hock, R., McNabb, R. W., Millan, R., Sommer, C., Braun, M. H., Malz, P., Maussion, F., Mouginot, J., Seehaus, T. C., and Shean, D. E. (2021). Distributed Global Debris Thickness Estimates Reveal Debris Significantly Impacts Glacier Mass Balance, Geophysical Research Letters, 48, https://doi.org/10.1029/2020GL091311.

748 Reznichenko, N., Davies, T., Shulmeister, J., and McSaveney, M. (2010). Effects of debris on ice-
749 surface melting rates: an experimental study, J. Glaciol., 56, 384–394,
750 https://doi.org/10.3189/002214310792447725.

751 Robertson, E. C. (1998). Thermal properties of rocks, United States Geological Survey, Open-File
752 Report 88-441, 106 pp.

753 Schaefli, B. and Huss, M. (2011). Integrating point glacier mass balance observations into
754 hydrologic model identification, Hydrol. Earth Syst. Sci., 15, 1227–1241,
755 https://doi.org/10.5194/hess-15-1227-2011.

756 Scherler, D., Wulf, H., and Gorelick, N. (2018). Global Assessment of Supraglacial Debris Cover
757 Extents, Geophys. Res. Lett., 45, 11798–11805, https://doi.org/10.1029/2018GL080158.

758 Steiner, J. F., Kraaijenbrink, P. D. A., and Immerzeel, W. W. (2021). Distributed melt on a debris-
759 covered glacier: field observations and melt modeling on the Lirung Glacier in the Himalaya,
760 Front. Earth Sci., 9, https://doi.org/10.3389/feart.2021.678375.

761 Tangborn, W. and Rana, B. (2000). Mass Balance and Runoff of the Partially Debris-Covered
762 Langtang Glacier, Debris-Covered Glaciers, edited by: Nakawa, M., Raymond, C. F., and
763 Fountain, A., IAHS Publication 264.

764 Tielidze, L. G., Bolch, T., Wheate, R. D., Kutuzov, S. S., Lavrentiev, I. I., and Zemp, M. (2020).
765 Supra-glacial debris cover changes in the Greater Caucasus from 1986 to 2014, The Cryosphere,
766 14, 585–598, https://doi.org/10.5194/tc-14-585-2020.

767 Verhaegen, Y., Huybrechts, P., Rybak, O., and Popovnin, V. V. (2020). Modelling the evolution
768 of Djankuat Glacier, North Caucasus, from 1752 until 2100 CE, The Cryosphere, 14, 4039–4061,
769 https://doi.org/10.5194/tc-14-4039-2020.

770 Verhaegen, Y., Huybrechts, P., Rybak, O., and Popovnin, V. V. (subm.). Quantifying supraglacial
771 debris-related melt-altering effects on the Djankuat Glacier, Russian Federation, Part 1:
772 comparison of surface energy and mass fluxes over clean ice and debris-covered terrain [in
773 review].

774 Verhaegen, Y. and Huybrechts, P. (subm.). Model code for surface energy and mass balance
775 modelling of clean ice and debris-covered ice on the Djankuat Glacier, Zenodo,
776 https://doi.org/10.5281/zenodo.7451031.

777 Wang, L., Li, Z., and Wang, F. (2011). Spatial distribution of the debris layer on glaciers of the
778 Tuomuer Peak, western Tian Shan. J. Earth Sci. 2011, 22, 528–538.
779 https://doi.org/10.1007/s12583-011-0205-6.

780 Wei, Y., Tandong, Y., Baiqing, X., and Hang, Z. (2010). Influence of supraglacial debris on
781 summer ablation and mass balance in the 24K Glacier, southeast Tibetan Plateau, Geografiska
782 Annaler: Series A, Physical Geography, 92, 353–360, https://doi.org/10.1111/j.1468-
783 0459.2010.00400.x.

784 WGMS (2022). Djankuat, North Caucasus, World Glacier Monitoring Service, available at:
785 https://wgms.ch/products_ref_glaciers/djankuat, last access: 17 November 2022.

786 Winter-Billington, A., Dadic, R., Moore, D., Flerchinger, G.N., Wagnon, P., and Banerjee, A.
787 (2022). Modelling debris-covered glacier ablation using the Simultaneous Heat and Water

788 transport model. Part 1: Model development and application to North Changri Nup, Frontiers in
789 Earth Science, 10, Article 796877, https://doi.org/10.3389/feart.2022.796877.